LANGMUIR

Atomistic Simulations of Biofouling and Molecular Transfer of a Cross-linked Aromatic Polyamide Membrane for Desalination

Md Symon Jahan Sajib, Ying Wei, Ankit Mishra, Lin Zhang, Ken-Ichi Nomura, Rajiv K. Kalia, Priya Vashishta, Aiichiro Nakano,* Sohail Murad,* and Tao Wei*

Read Online

ACCESS | Metrics & More | Article Recommendations | Supporting Information

ABSTRACT: Reverse osmosis through a polyamide (PA) membrane is an important technique for water desalination and purification. In this study, molecular dynamics simulations were performed to study the biofouling mechanism (i.e., protein adsorption) and nonequilibrium steady-state water transfer of a cross-linked PA membrane. Our results demonstrated that the PA membrane surface's roughness is a key factor of surface's biofouling, as the lysozyme protein adsorbed on the surface's cavity site displays extremely low surface diffusivity, blocking water passage, and decreasing water flux. The adsorbed protein undergoes secondary structural changes, particularly in the pressure-driven flowing conditions, leading to strong protein−surface interactions. Our simulations were able to present water permeation close to the experimental conditions with a pressure difference as low as 5 MPa, while all the electrolytes, which are tightly surrounded by hydration water, were effectively rejected at the membrane surfaces. The analysis of the self-intermediate scattering function demonstrates that the dynamics of water molecules coordinated with hydrogen bonds is faster inside the pores than during the translation across the pores. The pressure difference applied shows a negligible effect on the water structure and content inside the membrane but facilitates the transportation of hydrogen-bonded water molecules through the membrane's sub-nanopores with a reduced coordination number. The linear relationship between the water flux and the pressure difference demonstrates the applicability of continuum hydrodynamic principles and thus the stability of the membrane structure.
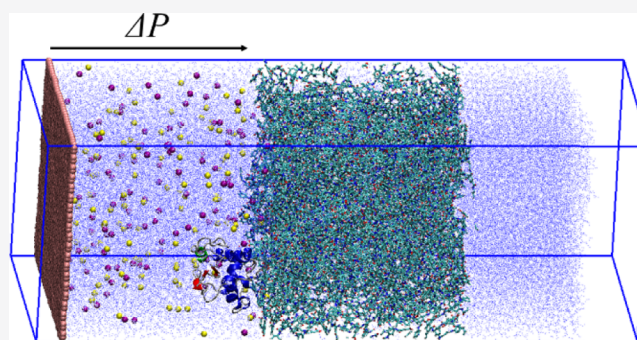

INTRODUCTION

Because of dramatic industrial development and the unprecedented growth of population, finding a viable desalination method of seawater or brackish water has been of great research interest and also a challenge. Reverse osmosis (RO) accounts for more than 50% of the currently installed capacity around the world because of its energy efficiency (over 50% thermodynamic efficiency), eco-friendliness, and ease of operation[1] over other desalination techniques. RO is a pressure driven process with differential permeability that favors water over the ions and impurities through a selective semipermeable membrane.[2] After Loeb and Sourirajan developed a method of making the RO membrane in the early 1960s,[3] it became a practical and feasible tool for water desalination. In 1969, Dupont developed the polyamide (PA) membrane, which, because of subsequent improvements in the years since, gained wide commercial success[4] for RO. To date, aromatic PA and cellulose acetate (CA) are the two best known polymers for the RO membrane.[5] The phase inversion method is used for preparing a CA RO membrane, whereas the PA RO membrane is fabricated via a polymerization process.[6−10] Through polymerization, a dense sub-nanoporous aromatic PA layer is formed with an average thickness ranging around 100−200 nm on the polysulfone support.[6−10] Because of lesser microbiological contamination, ease of large-scale fabrication, and more chemical stability than the CA-based membrane, PA thin-film membranes have been widely adopted.[2] PA also shows a salt rejection rate as high as >99%.[11,12] Despite development efforts for more than three decades, increasing polymer membrane efficiency continues to be an active research area. For example, the recently developed nanofiltration PA membrane with a unique Turing structure demonstrates enhanced transport properties in terms of both water permeability and water−salt selectivity.[13] However, achieving high water flux without sacrificing the high salt rejection still remains a challenge.[11]
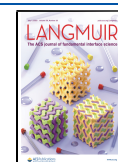
Understanding the membrane structure and the mechanism of water transport at the atomistic scale is essential to the design of efficient membranes. To complement experimental efforts,[14−21] atomistic molecular dynamics (MD) simulations have been employed to investigate sub-nanoporous polymer membranes[22−29] because of its ability to provide insights on spatial details at the atomic level at a range of time scales spanning from sub-nanoseconds to microseconds.[30−34] Atomistic MD simulations also have unique advantages in terms of quantitative analysis and can take into account the complicated chemistry and molecular structures of polymers and biomolecules, as well as the effects of the external environment.[30,35−37] Different aspects of the PA membrane were successfully studied with MD, such as the structural, dynamic, and dielectric properties of water confined by aromatic PA;[29,38] the water flux and the ion rejection;[2,11,23,36,39] the molecular transport phenomena;[22,36] and the membrane's microscopic structure.[22,36] In our previous study,[36] we developed a fully atomistic model of PA by a hierarchical cross-linking method, which proved to be an efficient method.[40,41] Our simulations[36] predicted three structural components (parallel stacked benzene rings, T-shaped benzene rings, and linearly bonded neighboring rings), which are the major factors for the membrane porosity. X-ray scattering experiments[42] have demonstrated the presence of the structural components of parallel stacking and T-shape. Both experiments[43] and simulations[36] showed that the majority of the pores in a polymer membrane have a radius of ∼0.20 nm, giving rise to the observed membrane selectivity for salt−water separation. Water molecules exhibit heterogeneous diffusivities inside the inhomogeneous polymer membrane.[36,44] More water molecules are found located adjacent to the polar carboxyl or amino groups and flow faster around benzene rings than polar carboxyl or amino groups.[11] Fast water permeation is observed through less cross-linked regions inside the membrane.[36]

Biofouling of the polymer membrane is an important factor to investigate. Such fouling can be caused by the adsorption of microorganisms, natural organic matter, and biomolecules, such as glucose, phenol, alginate, and proteins.[45,46] It can lead to a loss of water flux, an increase in RO system operating pressure, and increased cleaning frequency, thereby shortening membrane life.[46] Hence, the fouling mechanism between biomolecules and PA membrane from an atomistic perspective is worth investigating. Hughes and Gale's MD simulations[47] showed that glucose formed multiple hydrogen bonds with polymer functional groups after diffusing onto the membrane, while phenol not only adsorbed on the membrane surface but in some cases also diffused through the membrane pores, which they attributed to its hydrophobic nature. Leng et al. studied the fouling mechanism of alginate on the PA membrane, and their MD simulations showed that the ions (Na^+ and Ca^{2+}) can exhibit strong binding with the carboxylate groups of the PA surfaces.[46,48] In addition, extensive MD simulations have already been successfully performed to study and understand protein adsorption on polymers[32,49] and crystals.[50−53] Nevertheless, simulations of the protein biofouling mechanism for the PA membrane are still limited. A multiwalled carbon nanotube-PA nanocomposite (MWCNT-PA) membrane with a biofoulant BSA protein was studied by Takizawa et al., who found a stiffer, smoother, and more hydrophilic surface morphology which altogether results in weaker interactions between the membrane and BSA.[54] As previous studies[46−48,54] pointed to the existence of different fouling mechanisms as the diversity of the foulant increases, this serves as a strong motivation for studying the protein biofouling mechanism on PA by atomistic simulations in this work.

Although significant progress has been made in understanding water transport and salt rejection by the previous studies mentioned above, some issues still remain unresolved. Despite RO being a nonequilibrium pressure driven process, equilibrium MD (EMD) studies were commonplace to understand the structure and process.[22,25,26] Noncross-linked or partially cross-linked PA membranes were employed in the simulations, which are unable to represent a realistic system of a cross-linked membrane.[53,55] In studies with nonequilibrium MD simulations, very large pressure differences (more than 100 MPa)[11,23,27,56] were used. In experiments, the operating pressure is only 0.2−1.7 MPa for brackish water and 4−8.2 MPa for seawater.[57−59] Studies of nonequilibrium processes under a very high pressure difference using conventional MD can lead to biased results.

In this study, the biofouling mechanism and the nonequilibrium process in RO were investigated at a low pressure drop range (5−30 MPa). Lower pressure drop results in slower water transportation, and getting a significant transmembrane water flow is out of the current computational capacity. This is in the lowest range of pressure drops that can be reached by current simulation techniques to study a successful steady-state nonequilibrium process and significant transmembrane water flow. Also, to understand the chemical bonds' response of the membrane, a reactive MD simulation and relevant parameters are needed, which is currently outside of this MD study investigating biofouling mechanism, water flow, and saltwater separation. To study the protein biofouling mechanism of the PA membrane, a small-sized lysozyme was used as a model system to alleviate the computational load. The following sections of this paper include a description of the simulation methodology, results and discussion, and summary and conclusions. In the Results and Discussion section, membrane surface biofouling, molecular transfer of water through membrane, and water−salt separation are discussed. This study will provide insights for future development of a more efficient PA membrane for advanced RO operation and desalination.

■ METHODS

All EMD and nonequilibrium MD (NEMD) simulations were carried out using GROMACS package (version 4.6.5) in the NVT ensemble. CHARMM force field parameters have been successfully used to simulate the PA membrane as shown in the previously published papers.[36,55] In this work, the newest version of the CHARMM36 force field was adopted. For water molecules, the TIP3P model was used. The dynamic equations were integrated by using the leapfrog algorithm with a time step of 1 fs. The system was maintained at a temperature of 298.15 K with a Nosé−Hoover thermostat. The particle mesh Ewald summation was utilized to calculate the long-range electrostatic interactions, with a cutoff distance of 1.2 nm for the separation of the direct and reciprocal space. A spherical cutoff at 1.2 nm was imposed on LJ interactions. The long-range dispersion effect on energy and pressure was also included. A periodic boundary condition was applied to the system along the X and Y directions.

A PA membrane with a cross-linking degree of ∼70% was obtained from our previous study.[36] The water inside the membrane was kept as it is. For all the nonfouling NEMD cases, two water baths were added on both sides of the membrane. A single layer graphene wall has been added at the edge of the left water bath to enable the nonequilibrium process. The dimensions of the total system are 8.350

$\times$ 8.508 $\times$ 24.0 nm^3. Adequate ions (Na$^+$ and Cl$^-$) were added to maintain the ion concentration of sea water in the left water bath, and the graphene wall was subjected to the external acceleration to mimic the transmembrane pressure difference (Figure 1). The right water
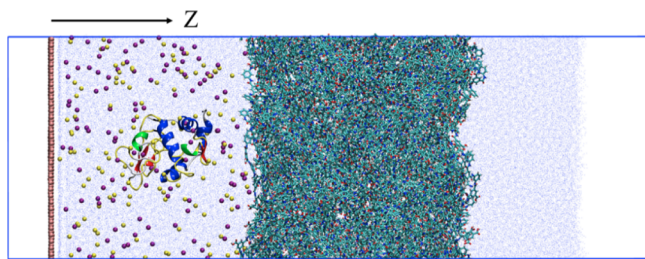
Figure 1. Initial configuration of NEMD of the PA membrane by pulling the graphene wall in the Z direction, which is normal to the graphene surface.

reservoir was open to the vacuum and contained no ions (Figure 1). Finally, four systems were simulated with different pressures (ΔP = 5, 10, 20, and 30 MPa) applied on the graphene wall.

$$P = \frac{a \cdot m}{A} \tag{1}$$

where P refers to pressure, A is the graphene surface area, m is the mass of the atoms that are being pulled, and a is the acceleration.

Here, to prevent the pressure driven movement of the membrane, only eight atoms were fixed on the Z direction, which is normal to the membrane surface. Compared to the total atom numbers (40907) of our membrane model, this is an insignificant amount which accounted for less than 0.02% of the total membrane atoms. All the fixed membrane atoms were chosen to be close to the water bath at the outlet and well distributed throughout the plane of the membrane to mimic the polysulfone support, usually placed at the bottom of the PA in experiments.

To simulate the biofouling of the PA membrane, an initial structure of a lysozyme (pdb:1HWA) was obtained from the Protein Data Bank website. The amino acid residues of histidine (His), arginine (Arg), and lysine (Lys) were protonated, whereas glutamate (Glu) and aspartate (Asp) were deprotonated which resulted in a net charge of +8e. For the biofouling case, the protein structure was solvated in the left water bath with an addition of 8 Cl$^-$ to neutralize the net charge of the protein (+8e), and then adequate Na$^+$ and Cl$^-$ ions were added to maintain the ion concentration of sea water (0.6 M). The water bath with the structure of lysozyme was first carefully relaxed for 10 ns before being placed on the left side of the membrane (Figure 1). The right water bath was the same as the fouling cases and contained no ions. In the initial configuration, the protein was observed to be at 0.8 nm in distance from the membrane surface. Finally, four systems with the same pressure difference as the fouling cases (ΔP = 5, 10, 20, and

30 MPa) were simulated to study biofouling in nonequilibrium conditions.

At steady state, the water flux, J, at a certain pressure difference was calculated through the amount of net rate water passing through a unit area of the membrane

$$J = \frac{\mathrm{d}N}{A \cdot \mathrm{d}t} \tag{2}$$

where A is the membrane surface's cross-sectional area; N is the net amount of water passed at a certain time; and t is the time. The number of net water difference (N) of the outlet water bath in reference to the initial configuration was recorded for each nanosecond. Using the linear region of the profile of N as a function of t, the steady-state flux was calculated.

The roughness of the membrane surface has been estimated by calculating the root-mean-square roughness,[68] R_q, as follows

$$R_q = \sqrt{\frac{\sum_{i=1}^{n} (Z_i - \overline{Z})^2}{n}} \tag{3}$$

where Z_i is the height of the exposed atoms on the film surface, $\overline{Z}$ represents the mean height exposed atoms and n is the total number of exposed atoms at a specific time step.

The center of mass (COM) calibration is a common practice in the equilibrium MD as a remedy of the "Flying ice cube" problem. It occurs mainly due to the numerical error build-up during the integral of the ODEs and is mainly associated with the Berendsen weak-coupling method and a Nosé−Hoover thermostat with very large (e.g., 20 fs) time steps. In our NEMD simulation, in which we used Nosé−Hoover with a standard time step (1 fs), COM recalibration has been removed. Otherwise, this might add an artificial error, which can significantly lower the water velocity in a NEMD simulation and result in a situation where the amount of pressure being applied on the system might be significantly smaller than what we originally applied externally and need an unrealistic amount of pressure to achieve any meaningful transmembrane water transfer in the simulation.

To study the steady-state nonequilibrium process of molecular transfer, extensive parallel computations were performed for cases of different pressure drops. For the cases without the addition of protein, the simulation time is 180 ns for ΔP = 30 MPa, 260 ns for ΔP = 20 MPa, 225 ns for ΔP = 10 MPa, and 260 ns for ΔP = 5 MPa. For the cases of biofouling, 200 ns simulations were performed for ΔP = 30 MPa, 205 ns for ΔP = 10 MPa, and 248 ns for ΔP = 5 MPa.

RESULTS AND DISCUSSION

Membrane Fouling Mechanism. Our simulated cross-linked PA membrane surface structure was observed to be highly uneven and rough. To quantify the roughness of the PA membrane, we calculated the root-mean-square roughness[68] (R_q) of the membrane surface close to the protein, which was
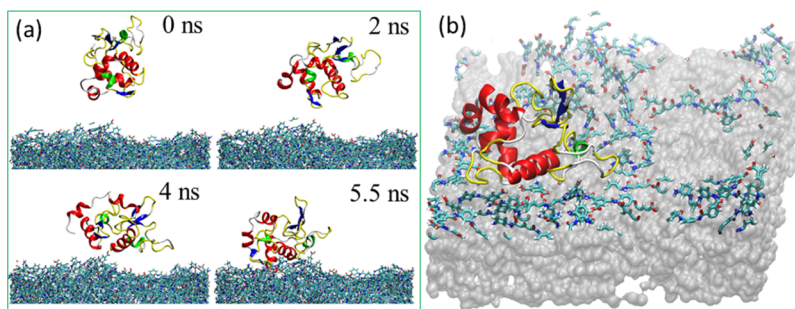
Figure 2. Lysozyme adsorption on the PA membrane: (a) lysozyme adsorption trajectory; (b) full adsorption of the lysozyme at 5.5 ns [top interfacial layer of membrane (top 0.4 nm) is rendered with a ball and stick model; the rest of the membrane is rendered with a gray colored ball model].
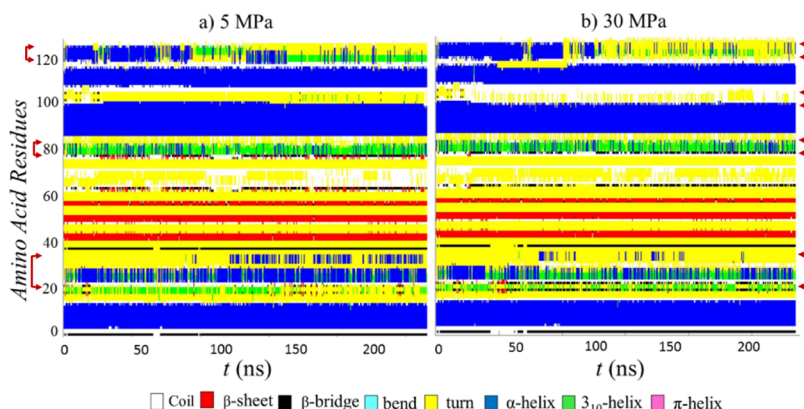
Figure 3. Time evolution of the secondary structure of an adsorbed lysozyme on the PA membrane surface for the case of 5 and 30 MPa pressure difference. Larger structural changes are denoted with red arrow marks.

0.44 nm. For a membrane with a total thickness of ∼8 nm, this is a large roughness. Figure S1 is rendered with the interfacial atoms of the membrane for a better understanding of the roughness of the membrane surface. Both of the high RMS roughness and Figure S1 established our membrane surface as a "peak and valley" model, which is similar to previous simulation and experimental observations.[62,63] The process of the lysozyme protein adsorption is monitored, as shown in Figure 2a. The lysozyme was initially placed at a distance of 0.8 nm from the membrane surface without the pressure difference applied. The protein was observed to reorient in the bulk and move toward the membrane surface. At around 4 ns, the protein started to contact the surface and was then fully adsorbed on a valley site of the membrane surface at ∼5.5 ns (Figure 2b). For further validation, four more simulations were performed to study the protein attachment process on the membrane, using different initial orientations and positions of the protein on the PA membrane surfaces. In all the simulations, the lysozyme was found to be adsorbed in a cavity site of the membrane, which confirms that the cavity sites are more prone to protein adsorption and also validates the important role of roughness in the biofouling mechanism. Our results are also in agreement with the previous experimental observations,[60,61] which showed that valleys or cavities on an irregular membrane surface are a "hotspot" for foulant attachment, which then leads to a reduced water flux. On the other hand, a smooth surface without cavities is less prone to biofouling as it can trap less foulants or hold suspended solids present in water.[60−62]

To understand the interactions between the lysozyme and the membrane, we examined the protein's landing site on the membrane. Hydrophilic residues (Arg21, Lys33, Gly71, Asn103, and Arg128) were closest to the membrane surface. Although the overall PA membrane surface exhibits hydrophilicity, it consists of mixing hydrophobic moieties (e.g., benzene rings) and the hydrophilic moieties (e.g., the polar atoms of N and O). Further studies in the future are desirable to reveal the correlation of protein attachment on the mixed hydrophobic/hydrophilic surfaces. Four other cases of simulation were performed for a validation purpose, where the hydrophilic residues were also found to be nearest to the surface after adsorption. Our results show that after 5.5 ns of the initial event of protein adsorption, protein−surface Lennard-Jones interaction energy (E_{LJ} = −250 kJ/mol) is one order of magnitude higher than the protein−surface

electrostatic interaction energy (E_{elc} = −50 kJ/mol). Few previous studies[25,48] referred to an "ionic bridge" model for the PA membrane and foulant interactions with the organic molecules of humic acids,[25,48] where ions such as Ca^{2+} and Na^+ can exhibit strong binding with carboxylate groups in the PA surface, leading to PA-alginate fouling.[25,48] For our case, no ion-mediated interactions were observed between the adsorbed protein and the PA membrane. Likewise, Gray and co-workers' study[63] of the interactions between the BSA protein and the PA membrane reported the absence of ionic bridge interactions. No π−π stacking interactions between the aromatic benzene rings of the PA membrane and the protein were detected, as lysozyme's residues with aromatic groups (Phe, Tyr, and Trp) tend to be far from the membrane surface. Further investigations are needed to confirm the role of ions in the biofouling mechanism by using different proteins in solutions with the addition of other electrolytes at different conditions.

To quantify the protein's structural deformation upon adsorption, two simulation works were performed to monitor the amino acid residues' secondary structures (Figure 3) of the adsorbed lysozyme and root-mean-square-displacement (RMSD) (Figure 4), with different pressure differences (ΔP = 5 and 30 MPa) applied to both sides of the reservoirs. Both simulations were started using the same configuration taken from the equilibrium conditions (Figure 2b). As shown in Figure 3, after the lysozyme is adsorbed onto the membrane at
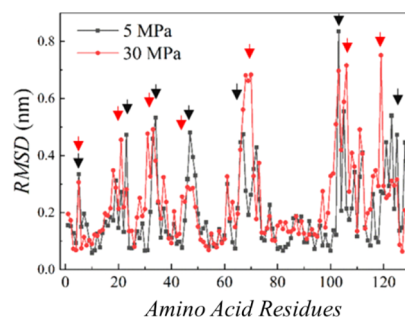
Figure 4. RMSD of amino acid residues for ΔP = 5 and 30 MPa. RMSD was computed using a protein's heavy backbone, excluding hydrogen atoms. The initial conformation of the lysozyme in the bulk water away from the surface was used as a reference to the computation of RMSD. Regions with a large RMSD are indicated by black arrows for 5 MPa and red arrows for 30 MPa.

~5.5 ns, several changes in the protein secondary structure were noticeable. At ΔP = 5 MPa, large changes were observed at Tyr20-Glu35, Asn77-Leu83, and Val120-Arg128 (Figure 3a). An additional change from turn to coil in the residues of Lys97-Trp108 was detected for (Figure 3b) ΔP = 30 MPa. These local areas of large secondary structural changes also correspond to the area around the protein adsorption site. These structural changes were identified during the initial stage of the protein adsorption (200−300 ns). The result shows significant structural changes for both cases (5 and 30 MPa) compared to their initial structure, but little difference among them with more structural changes occurring for 30 MPa. These large structural rearrangements were also evidenced by the larger RMSD at these regions around the hydrophilic amino residues (Arg21, Lys33, Gly71, Asn103, and Arg128) (Figure 4), which were in close proximity to the polymer membrane surfaces. Few other regions away from the surface around Arg5 and Thr47 also displayed a large change. Compared to the low-pressure difference at ΔP = 5 MPa, protein exhibited a larger RMSD (e.g., Gly67-Pro70 and Met105-Asp119) at ΔP = 30 MPa (Figure 4), which indicates more structural rearrangement because of the higher pressure. It is notable that despite the abundance of benzene rings in the PA membrane and the hydrophilic polar groups, which introduce large water content inside the membrane, the adsorbed lysozyme showed structural changes consequently increasing the protein's interactions with the polymer membrane surface (see Figure S2 in the Supporting Information). In contrast, previous studies showed that on the flexible azobenzene-terminated alkyl brush surfaces, the lysozyme exhibited relatively stable secondary structure.[53]

In our study, the lysozyme diffusivity on the membrane was computed by monitoring the mean square displacement of the protein's COM on the $X-Y$ plane using the time autocorrelation function as follows,

$$\mathcal{D}_{lat} = \lim_{\Delta t \to \infty} \frac{\langle [\mathbf{r}(t + \Delta t)] - \mathbf{r}(t)^2 \rangle}{4\Delta t} \qquad (4)$$

where $\mathbf{r}$ denotes the protein's COM position and t is the time.

The lysozyme diffusivity on the surface was found to be 1.49 × 10^{-8} cm^2/s. Comparison of the lysozyme diffusivity on other surfaces can reveal how much surface roughness and the morphology can affect the mobility of the lysozyme. For example, previous studies revealed the mobility of lysozymes (1.8 × 10^{-5} cm^2/s) on a plain graphene surface,[51] which is significantly higher than in our case. On the other hand, lysozyme on azobenzene-terminated alkyl brush surfaces, which are also uneven and rough, shows low mobility (2.42 × 10^{-9} cm^2/s)[53] similar to PA. This result demonstrates that the mobility of the protein surface is highly correlated with the morphology and surface roughness.

Water Dynamics. A steady flow of the water molecules over time after the initial period (Figure S3) in our simulations has been observed for all the applied pressure differences in cases without and with protein adsorption. Also, with more pressure being applied, water permeation increases (Figure S3), which shows our system's ability to facilitate steady-state nonequilibrium conditions.

The water flux (J) through a RO PA membrane can be represented by the Hagen−Poiseuille equation, which shows the relationship of J with the membrane's structural properties,

the fluid properties, and the operating conditions, for example, the pressure difference, temperature, and the salt concentration

$$J = \frac{\varepsilon r_p^2}{8\tau L\eta} (\Delta P - \Delta \pi) = \kappa (\Delta P - \Delta \pi) \qquad (5)$$

where ε stands for the surface porosity; r_p is the effective pore radius; τ is the pore tortuosity; L is the membrane effective thickness; and η is the water viscosity, which is mainly a function of temperature; κ is the water permeability; and $\Delta\pi$ represents the osmotic pressure, which can be estimated using the van't Hoff relationship, assuming the ideal solution

$$\Delta\pi = RT\Delta C \qquad (6)$$

where R is the ideal gas constant; T is the temperature; and ΔC is the concentration difference for reservoirs on both sides. Equation 5 shows a linear relationship between the flux and pressure drop, which is important to demonstrate the applicability of continuum hydrodynamic principles and thus the stability of the membrane structure. Although it is out of the scope of this study to investigate other macroscopic properties of the membrane and fluid, we calculated the pore size distribution (Figure S4) for both 5 and 30 MPa. The result shows that pressure drops within the range of 5−30 MPa have negligible effects on the pore size distribution (Figure S4) and the membrane thickness (Figure S5).

In our system, ΔC is 0.6 M for both Na$^+$ and Cl$^-$ ions, and, accordingly, $\Delta\pi$ is 2.974 MPa. At the same ΔC, we applied four pressure differences (ΔP = 5, 10, 20, and 30 MPa), which are larger than $\Delta\pi$, to investigate the pressure-driven nonequilibrium processes of the PA membrane without surface biofouling. Three more cases of pressure differences (ΔP = 5, 10, and 30 MPa) with the addition of a lysozyme molecule were investigated to study the biofouling effect on water permeation.

Figure 5 shows that the average molecular flux of the water displays a linear relationship with the increasing amount of
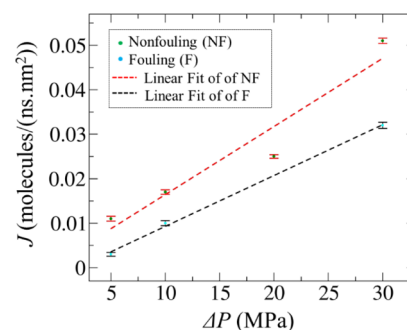
Figure 5. Average water flux (J) as a function of pressure difference (ΔP). Average water flux was calculated by calculating the slope of the net molecule number of waters. Three fluxes were calculated by considering net molecules passed over time (Figure S3a,b) after 80 ns, after 120 ns, and 160 ns. Then, the average flux and standard error of those three measurements at different times have been calculated.

pressure difference for both fouling and nonfouling cases. For all the fouling and nonfouling cases, the average flux is calculated by taking the slope of three different regions (from 80 ns, from 120 ns, and from 160 ns), as shown in Figure S3a,b. Also, the standard error of the average water flux is calculated and showed as an error bar in Figure 5. In the nonfouling case, the molecular flux was ~0.011 molecules ns^{-1}·
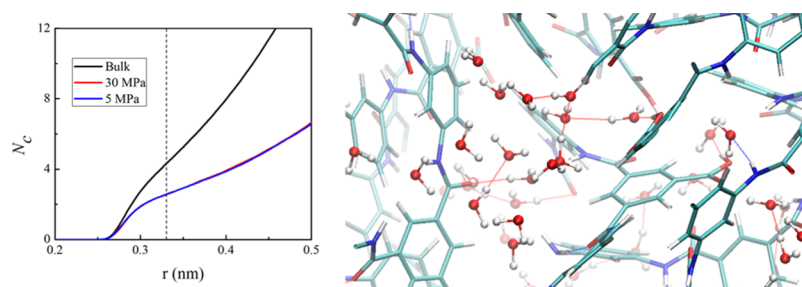
Figure 6. (a) Water coordination number (N_c) in the water bulk and inside the membrane under $\Delta P = 5$ and 30 MPa. The position at $r = 0.33$ nm is indicated by a black dashed line. (b) Snapshot of hydrogen bonds inside the membrane.

nm^{-2} for 5 MPa, which increased ($\sim$0.017 molecules ns^{-1}·nm^{-2}) with a pressure difference of 10 MPa. At 30 MPa, the molecular flux was recorded at 0.051 molecules ns^{-1}·nm^{-2}, which was around 5 times faster than the 5 MPa cases. By applying the linear fit on the flux, water permeability κ is estimated to be 0.0015 molecules ns^{-1} nm^{-2} MPa^{-1}, which suggests that with every unit (MPa) increase of pressure drop, the molecular flux will increase by a factor of 0.0015. The linear relationship of the flux and pressure difference also indicates the stability of the overall membrane structure as a function of the structural factors of τ, r_p, and L (see eq 5) throughout the pressure differences till 30 MPa. This was also verified by the fact that both pore size distribution and the membrane thickness remained largely unchanged with the increasing pressure difference till 30 MPa.

In some previous studies,[11,23,27,56] large pressure differences, which are experimentally not feasible (100−270 MPa), were applied and then the value of the water flux at the lower ΔP was predicted by extrapolating the data of $J - \Delta P$. Our simulations can mimic the process of water permeation at low pressure differences close to the industrial conditions, for example, $\Delta P = 5$ MPa, to establish a direct correlation between the flux and the pressure difference. In our study, for a 5 MPa pressure difference, the membrane thickness was $\sim$8 nm, while the water flux was 0.011 molecules ns^{-1} nm^{-2}, which is close to the experimental range[11] of 0.026−0.107 molecules ns^{-1} nm^{-2}. More studies on the effect of the membrane thickness on water flux will be carried out in our future investigations.

We should stress the fact that in our NEMD simulations, removal of the motion of the COM was avoided. In general, such a correction is a common practice in MD simulations to avoid the overall movement (icy moment) of the whole system caused by the round-off errors of numerical computations. The translational and rotational motions of the COM for the entire system have been usually considered as zero and the overall momentum is conserved, if no external force or field is applied. For a system like ours in a nonequilibrium steady state, if performed as in the general practice, the COM recalibration can add an artificial error to the velocities of the water molecules; hence, the effect of the external pressure difference will not be correctly applied, which can lead to an unrealistic high-pressure difference. In our simulations, the membrane surface was constrained by constraining several atoms of the sub-nanoporous membrane (see the section of Methods). This strategy prevents the shifting of an unrealistic icy motion of the whole system and can also present the water flow at the nonequilibrium steady state at a much lower pressure difference, which is close to the experimental/industrial operating conditions. Whereas other studies required higher

pressures to observe water transportation through the membrane, which is practically not viable.[11,23,27,56]

We also studied the effect of biofouling on the water transportation at $\Delta P = 5$, 10, and 30 MPa in the nonequilibrium steady state. Like the nonfouling cases, the flux increases in a linear fashion as the pressure increases. As expected, the average flux in all three biofouling cases were lesser than their fouling cases, and with the pressure difference increasing, the absolute difference of the molecular flux between fouling and nonfouling also rises significantly. For the 5 MPa case, the flux was recorded as 0.004 molecules ns^{-1}·nm^{-2}, which was lesser than half of the case without biofouling. At 30 MPa, the water flux was recorded as 0.0305 molecules ns^{-1}·nm^{-2}, which was significantly less than the case without biofouling (0.051 molecules ns^{-1}·nm^{-2}). To quantify as an overall trend of the flux drop permeability, k for the biofouling case was estimated at 0.0011 molecules ns^{-1}·nm^{-2}, which is 27% smaller than in the nonfouling cases. In our computation of the water flux for the surfaces adsorbed with a lysozyme protein, we used the same entire cross-surface area as that of the nonbiofouling surfaces in order to show the biofouling effect on the water flux. Therefore, the decrease in the water flux is mainly attributed to the reduction of the membrane surface area available for water permeation, as the lysozyme protein was adsorbed on the membrane and less water transferred across the membrane surface. It is notable that the adsorbed protein can also modify the membrane surface's physical properties, such as the polarity and charge distribution, and affect water permeation. Further studies are desired to investigate such more sophisticated factors that arise from the adsorbed foulers on membrane surfaces.

To characterize the water structure at different conditions, we calculated the water coordination number (N_c), which quantifies the number of the neighboring water molecules surrounding a water molecule at a certain radial distance (r). As shown in Figure 5, N_c is higher in bulk water than inside the membrane for both cases ($\Delta P = 5$ and 30 MPa). Water molecules inside the membrane were trapped inside the cage-like structure of the membrane (Figures 6 and S6 in Supporting Information). Our previous study showed[36] that for water molecules inside the membrane, only the first hydration shell exists, while the second hydration shell disappears. In this study, the bottom of the first hydration shell was used as a cutoff distance ($r = 0.33$ nm) to compute N_c. The bulk water coordination number was recorded as 4.5, while inside the membrane it was $\sim$2.8 for both 5 and 30 MPa. This result suggests that the average number of water molecules in the water's first hydration shell inside the membrane is 38% less than bulk water. The N_c of water inside the membrane at nonequilibrium conditions is close to

the value of the membrane at equilibrium solvation conditions because of the hydrogen bonding inside the pores of the polymer membrane (Figure 6). This indicates that, although the pressure drop increases the water flux, it bears no significant effect on the water structure inside the membrane.

To describe the dynamics of water molecules in the interior area of the membrane, we calculated the self-intermediate scattering function (SISF), which is the self-part of the Fourier transform of the distribution function of the single-water positions in space

$$F_s(\boldsymbol{k}, t) = \frac{1}{N} \sum_{i=1}^{N} \langle \cos(\boldsymbol{k} \cdot [\boldsymbol{r}_i(t) - \boldsymbol{r}_i(0)]) \rangle \tag{7}$$

where N is the number of the oxygen atoms of water; $\boldsymbol{k}$ represents the wavevector; $\boldsymbol{r}_i(0)$ is the initial position vector of the i-th oxygen atom; $\boldsymbol{r}_i(t)$ is the position vector of the i-th oxygen atom at time t; and the angular brackets stand for the time autocorrelation function. Our previous study[36] showed that the majority of the pores' diameters are ~4 Å. We first computed $F_s(\boldsymbol{k},t)$ using the simulation of the solvated PA membrane at the equilibrium conditions obtained from our previous studies.[36] Figure 7 shows the SISF at three different
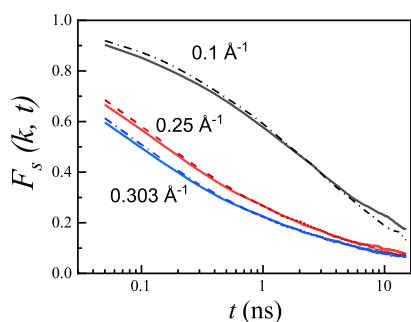
Figure 7. SISF $F_s(\boldsymbol{k},t)$ of oxygen atoms of water molecules inside the membrane at wavenumbers $\boldsymbol{k}$ = 0.1, 0.25, and 0.303 Å^{-1} for the membrane at equilibrium conditions (straight lines) and the nonequilibrium with ΔP = 0.5 MPa (dash-dot lines).

wavenumbers: $\boldsymbol{k}$ = 0.303, 0.25, and 0.1 Å^{-1}, which correspond to the hydrogen bond length, the diameter of major pores, and the length more than the maximum pore size, respectively. The decay of $F_s(\boldsymbol{k},t)$ can be described with a stretched exponential relaxation function, that is, the Kohlrausch–Williams–Watts (KWW) function

$$F_s(\boldsymbol{k}, t) = f_Q \exp\left(-\left(\frac{t}{\tau}\right)^{\beta}\right) \tag{8}$$

where f_Q is the Debye–Waller factor; τ represents the associated relaxation time; and β is the stretching parameter (see Table 1 and Figure S7 in the Supporting Information). Given small displacement distances, which are less or equal to the size of major pores, both $F_s(\boldsymbol{k},t)$ curves of $\boldsymbol{k}$ = 0.303 and 0.25 Å^{-1} show a slight difference (Figure 7 and Table 1). Both of them exhibit fast decay with small relaxation time (τ = 0.343 and 0.208 ns, respectively) and small stretching parameters (β = 0.262 and 0.245, respectively), which indicates the fast dynamics of coordinated water molecules inside the pores. After the initial quick decrease in $F_s(\boldsymbol{k},t)$, a slower decrease follows because of the slow dynamics of water molecules, which are highly trapped inside the pores of the membrane.

Table 1. Comparison of the Fitting Parameters of the Stretching Exponential Functions at the Equilibrium State and the Nonequilibrium State With ΔP = 0.5 MPa

k		f_Q	τ (ns)	β
0.1 Å^{-1}	equilibrium	1.068	3.22	0.399
	ΔP = 0.5 MPa	1.046	3.22	0.468
0.25 Å^{-1}	equilibrium	1.034	0.344	0.262
	ΔP = 0.5 MPa	1.034	0.338	0.280
0.303 Å^{-1}	equilibrium	1.021	0.208	0.245
	ΔP = 0.5 MPa	1.025	0.218	0.252

For a larger displacement ($\boldsymbol{k}$ = 0.1 Å^{-1}), $F_s(\boldsymbol{k},t)$ displays a much slower decrease (τ = 3.22 ns), and a larger stretching parameter (β = 0.399) is detected (Figure 7 and Table 1). The slow decay is attributed to the longer time scale for water diffusion across the steric barrier of different pores. Similar dependency of $F_s(\boldsymbol{k},t)$ of the water molecules on the pore size or wave numbers has also been reported in previous studies.[64,65]

For the purpose of comparison, the SISF was also used to characterize the water dynamics in the interior area of the membrane under nonequilibrium conditions (ΔP = 0.5 MPa) (Figure 7). Table 1 and Figure S7 in the Supporting Information compare the results of simulations and the curve fitting. The comparison shows that for a larger displacement ($\boldsymbol{k}$ = 0.1 Å^{-1}), the pressure difference introduces a larger effect on the value of the stretching parameter β, compared to the small displacements ($\boldsymbol{k}$ = 0.303 and 0.25 Å^{-1}). It suggests that the pressure gradient helps water molecules overcome the energy barrier and transport across polymer membrane pores.

Salt and Water Separation. To understand the salt rejection performance of the membrane under nonequilibrium conditions, the density profiles of the membrane, water, and ions across the box for varying pressure differences (ΔP = 5, 10, 20, and 30 MPa) were monitored. Figure 8a compares the density distribution of different components in our simulation system for the case with a pressure drop of 5 MPa. It is notable that the densities shown in Figure 8a do not present the real densities. They were computed based on the total volume without taking into account the polymer atoms' exclusion volume. The ion concentration decreases at the polymer–water interface from the bulk value to zero. The coordination numbers of Na$^+$ and Cl$^-$ ions at the interface were computed using a cutoff distance of the width of the ion's first hydration shell: 4 Å for Na$^+$ and 3.8 Å for Cl$^-$. The numbers of coordinated water for Cl$^-$ and Na$^+$ ions are ~7 and ~6, respectively. Both of these interfacial values are the same as the values of ions in bulk water.[66,67] It suggests that an electrolyte of Na$^+$ or Cl$^-$ in the interface is surrounded tightly by its hydration water shell just like in the bulk. These ions, strongly surrounded by water layers, result in a total size larger than the membranes' pores [average pores ~0.2 nm (Figure S4)]. Thus, hydrated ions are blocked on the sub-nanoporous membrane surface (Figure 8a,b) because of their size and strong interactions with hydration water. External pressure difference and thermal forces cannot remove the hydration water surrounding the ions. Previous studies[36] showed the role of stronger affinity of water–ion than water–water to block the hydrated ions on the membrane interface, while letting the water pass through the membrane. During the entire course of simulations, no ions are detected to pass through the membrane. Even with the increase of ΔP, the membrane still
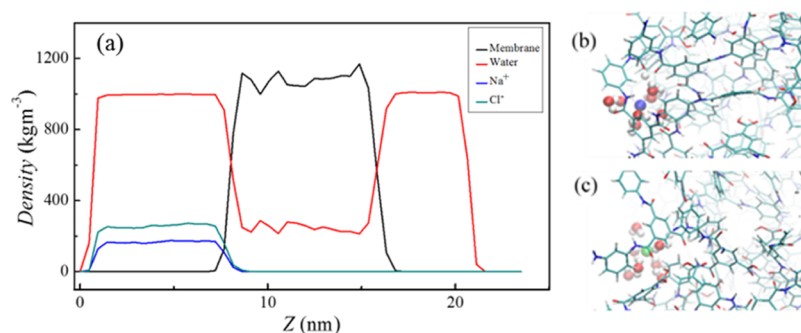
Figure 8. (a) Density distribution of the PA membrane, water, and ions (Na^+ and Cl^-); (b) snapshot of hydrated Na^+ ion on the PA membrane surface; and (c) snapshot of Cl^- ions on the PA membrane surface. The configurations within the last nanosecond were used to compute the average density distribution at ΔP = 5 MPa. It should be noted that the density is defined as the mass divided by the total volume at the Z position in the space. Note: the density was computed using the whole volume without taking into account the polymer exclusion volume.
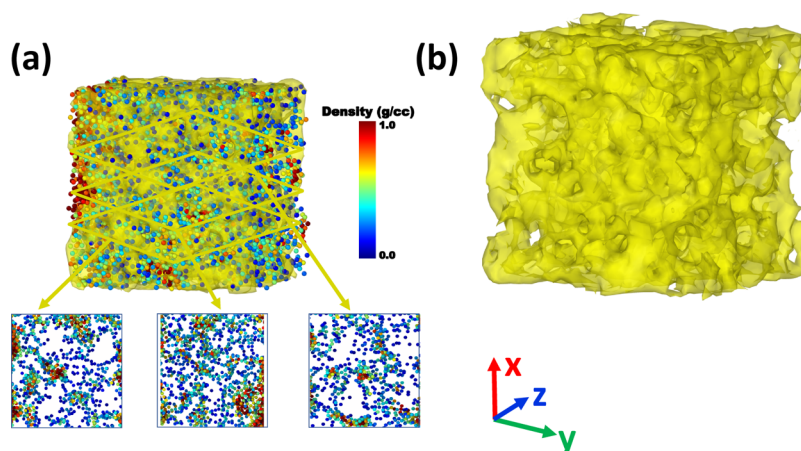
Figure 9. (a) Real water density distribution inside the PA membrane. The water molecules are color coded by their density, and the three slices show the density distribution of water molecules with increasing distance in X direction. (b) Pore structure of the membrane drawn using the construction of surface mesh with a probe sphere of radius 3 Å shows the porous nature of the membrane.

blocks all the ions at its interface (see the case of 30 MPa in Figure S6 in Supporting Information).

Figure 8a also shows negligible increase in the water content at the membrane interior area, and the swelled membrane thickness remained ∼9.6 nm, which is the same as that of the equilibrium solvation.[36] While increasing pressure difference transporting more water through the membrane, there is no significant change in the membrane density and thickness (see Figure S5 in the Supporting Information) and water content, which are different from the other studies,[56] detected using high ΔP (150 MPa). This can be attributed to the membrane's unchanged pore size distribution till 30 MPa (Figure S4 in the Supporting Information), which also indicates that no significant changes occurred in the membrane's internal free volume.

To further quantify water density distribution across the PA membrane, we computed real water density using Voronoi tessellation[64] excluding the PA membrane atoms. Voronoi cells were drawn around the oxygen atoms of water molecules excluding the PA membrane atoms. Real water density was calculated by dividing the mass of a water molecule with the volume of its Voronoi cell. Figure 9 shows high bulk density of water molecules (i.e., red color) mostly near polymer−water interfaces. Water distribution inside the PA membrane is highly heterogeneous as a result of the inhomogeneous membrane structure.

■ SUMMARY AND CONCLUSIONS

In this study, we have studied the pressure driven non-equilibrium steady-state process of a fully atomistic model of a PA membrane using atomistic MD simulations. Our results showed that the interfacial roughness is crucial to protein attachment, which results in a decrease of the water flux through the membrane. The adsorbed protein undergoes secondary structural changes and displays low mobility on the membrane surface. The water flux increases proportionally to the pressure difference (5−30 MPa), indicating that the internal structure of the membrane remains largely unchanged. Our simulations show that at the nonequilibrium conditions, hydrogen-bonded water molecules can permeate through a sub-nanoporous membrane driven by the pressure drop, although they are less coordinated inside the pores. In contrast, the passage of ions, which are tightly surrounded by water in the first-hydration shell, are still blocked at the membrane surface. Water molecules are trapped inside the cage-like structure of the membrane and display a highly heterogeneous density distribution. The SISF analyses of water dynamics showed that membrane pore sizes have a strong effect on the water dynamics inside the pores. Water exhibits fast dynamics inside a pore, whereas the trans-pore diffusion takes a longer time. The analysis of the water's coordination number indicates that the increasing pressure difference does not have any significant effect on the neighboring water

hydrogen bonding. It should be stressed that in this study, we were able to study the nonequilibrium process and properties in a pressure difference as low as 5 MPa, which is within the range of experimental conditions. Also, previous studies of biofouling mechanisms on the PA interface at the atomistic scale are far from adequate. Our study is an attempt to provide new and more precise insights on PA membranes by addressing both issues. This fundamental study will help the design of a much more efficient antibiofouling membrane for desalination.

■ ASSOCIATED CONTENT

ⓢ Supporting Information

The Supporting Information is available free of charge at https://pubs.acs.org/doi/10.1021/acs.langmuir.0c01308.

> Interface of the PA membrane; interaction energy (i.e., the sum of the Lennard-Jones and electrostatic energies) of protein and membrane surfaces; net molecule number of waters passed through membrane for different pressure; pore size distribution of the PA membrane at ΔP = 5, 30 MPa and equilibrium; density distribution at ΔP = 30 MPa without the addition of protein; water molecules shown in red & white are shown trapped around the PA membrane in a cage-like structure; and comparison of the original simulation data (circle symbols) and the curve fitting data (line) of SISF $F_s(\mathbf{k},t)$ (PDF)

■ AUTHOR INFORMATION

Corresponding Authors

Aiichiro Nakano − Mork Family Department of Chemical Engineering & Materials Science, Collaboratory for Advanced Computing and Simulations, Department of Physics & Astronomy, Department of Computer Science, and Department of Biological Sciences, University of Southern California, Los Angeles, California 90007, United States; ⓘ orcid.org/0000-0003-3228-3896; Email: anakano@usc.edu

Sohail Murad − Department of Chemical Engineering, Illinois Institute of Technology, Chicago, Illinois 60616, United States; ⓘ orcid.org/0000-0002-1486-0680; Email: smurad1@iit.edu

Tao Wei − Chemical Engineering Department, Howard University, Washington, District of Columbia 20059, United States; ⓘ orcid.org/0000-0001-6888-1658; Email: tao.wei@howad.edu

Authors

Md Symon Jahan Sajib − Chemical Engineering Department, Howard University, Washington, District of Columbia 20059, United States

Ying Wei − School of Information Science and Technology, Xiamen University, Tan Kah Kee College, Zhangzhou, Fujian 363105, China

Ankit Mishra − Mork Family Department of Chemical Engineering & Materials Science, University of Southern California, Los Angeles, California 90007, United States

Lin Zhang − Engineering Research Center of Membrane and Water Treatment of MOE, College of Chemical and Biological Engineering, Zhejiang University, Hangzhou 310027, China; ⓘ orcid.org/0000-0002-1337-2538

Ken-Ichi Nomura − Mork Family Department of Chemical Engineering & Materials Science and Collaboratory for Advanced Computing and Simulations, University of Southern California, Los Angeles, California 90007, United States

Rajiv K. Kalia − Mork Family Department of Chemical Engineering & Materials Science, Collaboratory for Advanced Computing and Simulations, Department of Physics & Astronomy, and Department of Computer Science, University of Southern California, Los Angeles, California 90007, United States

Priya Vashishta − Mork Family Department of Chemical Engineering & Materials Science, Collaboratory for Advanced Computing and Simulations, Department of Physics & Astronomy, and Department of Computer Science, University of Southern California, Los Angeles, California 90007, United States; ⓘ orcid.org/0000-0003-4683-429X

Complete contact information is available at:
https://pubs.acs.org/10.1021/acs.langmuir.0c01308

Notes

The authors declare no competing financial interest.

■ ACKNOWLEDGMENTS

■ REFERENCES

(1) Bennett, A. 50th Anniversary: Desalination: 50 years of progress. *Filtr. Sep.* **2013**, *50*, 32−39.

(2) Zhang, N.; Chen, S.; Yang, B.; Huo, J.; Zhang, X.; Bao, J.; Ruan, X.; He, G. Effect of hydrogen-bonding interaction on the arrangement and dynamics of water confined in a polyamide membrane: A molecular dynamics simulation. *J. Phys. Chem. B* **2018**, *122*, 4719−4728.

(3) Loeb, S.; Sourirajan, S. Sea water demineralization by means of an osmotic membrane. *Adv. Chem. Ser.* **1962**, *38*, 117−132.

(4) Hoehn, H. H. Aromatic Polyamide Membranes. *Materials Science of Synthetic Membranes*; American Chemical Society, 1985; Vol. 269; pp 81−98.

(5) Ghosh, A.; Bindal, R.; Prabhakar, S.; Tewari, P. Composite polyamide reverse osmosis (RO) membranes−recent developments and future directions. *BARC Newsl.* **2011**, *321*, 43−51.

(6) Hunter, W. Remediation of drinking water for rural populations. *Nitrogen in the Environment*; Elsevier, 2008; pp 597−621.

(7) Veerababu, P.; Vyas, B. B.; Singh, P. S.; Ray, P. Limiting thickness of polyamide−polysulfone thin-film-composite nanofiltration membrane. *Desalination* **2014**, *346*, 19−29.

(8) Antony, A.; Leslie, G. Degradation of polymeric membranes in water and wastewater treatment. In *Advanced Membrane Science and Technology for Sustainable Energy and Environmental Applications*, Basile, A., Nunes, S. P., Eds.; Woodhead Publishing, 2011; pp 718−745.

(9) Al-Hobaib, A. S.; Al-sheetan, K. M.; Shaik, M. R.; Al-Andis, N. M.; Al-Suhybani, M. Characterization and evaluation of reverse osmosis membranes modified with Ag_2O nanoparticles to improve performance. *Nanoscale Res. Lett.* **2015**, *10*, 379.

(10) Khorshidi, B.; Thundat, T.; Fleck, B. A.; Sadrzadeh, M. Thin film composite polyamide membranes: parametric study on the influence of synthesis conditions. *RSC Adv.* **2015**, *5*, 54985−54997.

(11) Song, Y.; Xu, F.; Wei, M.; Wang, Y. Water flow inside polamide reverse osmosis membranes: A non-equilibrium molecular dynamics study. *J. Phys. Chem. B* **2017**, *121*, 1715−1722.

(12) Bing, S.; Wang, J.; Xu, H.; Zhao, Y.; Zhou, Y.; Zhang, L.; Gao, C.; Hou, L. a. Polyamide thin-film composite membrane modified with persulfate for improvement of perm-selectivity and chlorine-resistance. *J. Membr. Sci.* **2018**, *555*, 318−326.

(13) Tan, Z.; Chen, S.; Peng, X.; Zhang, L.; Gao, C. Polyamide membranes with nanoscale Turing structures for water purification. *Science* **2018**, *360*, 518−521.

(14) Khorshidi, B.; Thundat, T.; Fleck, B. A.; Sadrzadeh, M. A novel approach toward fabrication of high performance thin film composite polyamide membranes. *Sci. Rep.* **2016**, *6*, 22069.

(15) Saleh, T. A.; Gupta, V. K. Synthesis and characterization of alumina nano-particles polyamide membrane with enhanced flux rejection performance. *Sep. Purif. Technol.* **2012**, *89*, 245−251.

(16) Shintani, T.; Matsuyama, H.; Kurata, N. Development of a chlorine-resistant polyamide reverse osmosis membrane. *Desalination* **2007**, *207*, 340−348.

(17) Hurwitz, G.; Guillen, G. R.; Hoek, E. M. V. Probing polyamide membrane surface charge, zeta potential, wettability, and hydro-philicity with contact angle measurements. *J. Membr. Sci.* **2010**, *349*, 349−357.

(18) Huang, H.; Qu, X.; Ji, X.; Gao, X.; Zhang, L.; Chen, H.; Hou, L. Acid and multivalent ion resistance of thin film nanocomposite RO membranes loaded with silicalite-1 nanozeolites. *J. Mater. Chem. A* **2013**, *1*, 11343−11349.

(19) Qiu, S.; Wu, L.; Zhang, L.; Chen, H.; Gao, C. Preparation of reverse osmosis composite membrane with high flux by interfacial polymerization of MPD and TMC. *J. Appl. Polym. Sci.* **2009**, *112*, 2066−2072.

(20) Dong, H.; Wu, L.; Zhang, L.; Chen, H.; Gao, C. Clay nanosheets as charged filler materials for high-performance and fouling-resistant thin film nanocomposite membranes. *J. Membr. Sci.* **2015**, *494*, 92−103.

(21) Lin, S.; Li, Y.; Zhang, L.; Chen, S.; Hou, L. a. Zwitterion-like, charge-balanced ultrathin layers on polymeric membranes for antifouling property. *Environ. Sci. Technol.* **2018**, *52*, 4457−4463.

(22) Harder, E.; Walters, D. E.; Bodnar, Y. D.; Faibish, R. S.; Roux, B. Molecular dynamics study of a polymeric reverse osmosis membrane. *J. Phys. Chem. B* **2009**, *113*, 10177−10182.

(23) Shen, M.; Keten, S.; Lueptow, R. M. Rejection mechanisms for contaminants in polyamide reverse osmosis membranes. *J. Membr. Sci.* **2016**, *509*, 36−47.

(24) Yoshioka, T.; Kotaka, K.; Nakagawa, K.; Shintani, T.; Wu, H.-C.; Matsuyama, H.; Fujimura, Y.; Kawakatsu, T. Molecular Dynamics Simulation Study of Polyamide Membrane Structures and RO/FO Water Permeation Properties. *Membranes* **2018**, *8*, 127.

(25) Xiang, Y.; Liu, Y.; Mi, B.; Leng, Y. Molecular dynamics simulations of polyamide membrane, calcium alginate gel, and their interactions in aqueous solution. *Langmuir* **2014**, *30*, 9098−9106.

(26) Kolev, V.; Freger, V. Hydration, porosity and water dynamics in the polyamide layer of reverse osmosis membranes: A molecular dynamics study. *Polymer* **2014**, *55*, 1420−1426.

(27) Ding, M.; Szymczyk, A.; Ghoufi, A. On the structure and rejection of ions by a polyamide membrane in pressure-driven molecular dynamics simulations. *Desalination* **2015**, *368*, 76−80.

(28) Liyana-Arachchi, T. P.; Sturnfield, J. F.; Colina, C. M. Ultrathin molecular-layer-by-layer polyamide membranes: insights from atom-istic molecular simulations. *J. Phys. Chem. B* **2016**, *120*, 9484−9494.

(29) Ding, M.; Szymczyk, A.; Goujon, F.; Soldera, A.; Ghoufi, A. Structure and dynamics of water confined in a polyamide reverse-osmosis membrane: A molecular-simulation study. *J. Membr. Sci.* **2014**, *458*, 236−244.

(30) Vemparala, S.; Kalia, R. K.; Nakano, A.; Vashishta, P. Electric field induced switching of poly (ethylene glycol) terminated self-assembled monolayers: A parallel molecular dynamics simulation. *J. Chem. Phys.* **2004**, *121*, 5427−5433.

(31) Vemparala, S.; Karki, B. B.; Kalia, R. K.; Nakano, A.; Vashishta, P. Large-scale molecular dynamics simulations of alkanethiol self-assembled monolayers. *J. Chem. Phys.* **2004**, *121*, 4323−4330.

(32) Wei, T.; Carignano, M. A.; Szleifer, I. Lysozyme adsorption on polyethylene surfaces: why are long simulations needed? *Langmuir* **2011**, *27*, 12074−12081.

(33) Hinkle, K. R.; Jameson, C. J.; Murad, S. Transport of vanadium and oxovanadium ions across zeolite membranes: a molecular dynamics study. *J. Phys. Chem. C* **2014**, *118*, 23803−23810.

(34) Floess, J. K.; Murad, S. Molecular simulations of the competitive adsorption of siloxanes and water on amorphous silica surfaces as a function of temperature. *Chem. Phys. Lett.* **2011**, *516*, 216−219.

(35) van der Munnik, N. P.; Sajib, M. S. J.; Moss, M. A.; Wei, T.; Uline, M. J. Determining the Potential of Mean Force for Amyloid-β Dimerization: Combining Self-Consistent Field Theory with Molecular Dynamics Simulation. *J. Chem. Theory Comput.* **2018**, *14*, 2696−2704.

(36) Wei, T.; Zhang, L.; Zhao, H.; Ma, H.; Sajib, M. S. J.; Jiang, H.; Murad, S. Aromatic polyamide reverse-osmosis membrane: An atomistic molecular dynamics simulation. *J. Phys. Chem. B* **2016**, *120*, 10311−10318.

(37) Wei, T.; Huang, T.; Qiao, B.; Zhang, M.; Ma, H.; Zhang, L. Structures, Dynamics, and Water Permeation Free Energy across Bilayers of Lipid A and Its Analog Studied with Molecular Dynamics Simulation. *J. Phys. Chem. B* **2014**, *118*, 13202−13209.

(38) Ding, M.; Ghoufi, A.; Szymczyk, A. Molecular simulations of polyamide reverse osmosis membranes. *Desalination* **2014**, *343*, 48−53.

(39) Ebro, H.; Kim, Y. M.; Kim, J. H. Molecular dynamics simulations in membrane-based water treatment processes: A systematic overview. *J. Membr. Sci.* **2013**, *438*, 112−125.

(40) Liu, Y.-l.; Xiao, K.; Zhang, A.-q.; Wang, X.-m.; Yang, H.-w.; Huang, X.; Xie, Y. F. Exploring the interactions of organic micropollutants with polyamide nanofiltration membranes: A molecular docking study. *J. Membr. Sci.* **2019**, *577*, 285−293.

(41) Wang, Z.; Xiao, K.; Wang, X.-m. Role of coexistence of negative and positive membrane surface charges in electrostatic effect for salt rejection by nanofiltration. *Desalination* **2018**, *444*, 75−83.

(42) Fu, Q.; Verma, N.; Ma, H.; Medellin-Rodriguez, F. J.; Li, R.; Fukuto, M.; Stafford, C. M.; Hsiao, B. S.; Ocko, B. M. Molecular Structure of Aromatic Reverse Osmosis Polyamide Barrier Layers. *ACS Macro Lett.* **2019**, *8*, 352−356.

(43) Kim, S. H.; Kwak, S.-Y.; Suzuki, T. Positron Annihilation Spectroscopic Evidence to Demonstrate the Flux-Enhancement Mechanism in Morphology-Controlled Thin-Film-Composite (TFC) Membrane. *Environ. Sci. Technol.* **2005**, *39*, 1764−1770.

(44) Cui, F.; Chen, W.; Kong, X.; Liu, L.; Shi, C.; Li, Y. Anomalous Dynamics of Water in Polyamide Matrix. *J. Phys. Chem. B* **2019**, *123*, 3086.

(45) Matin, A.; Khan, Z.; Zaidi, S. M. J.; Boyce, M. C. Biofouling in reverse osmosis membranes for seawater desalination: phenomena and prevention. *Desalination* **2011**, *281*, 1−16.

(46) Ridgway, H. F.; Orbell, J.; Gray, S. Molecular simulations of polyamide membrane materials used in desalination and water reuse applications: Recent developments and future prospects. *J. Membr. Sci.* **2017**, *524*, 436−448.

(47) Hughes, Z. E.; Gale, J. D. Molecular dynamics simulations of the interactions of potential foulant molecules and a reverse osmosis membrane. *J. Mater. Chem.* **2012**, *22*, 175−184.

(48) Xiang, Y.; Liu, Y.; Mi, B.; Leng, Y. Hydrated polyamide membrane and its interaction with alginate: a molecular dynamics study. *Langmuir* **2013**, *29*, 11600−11608.

(49) Wei, T.; Carignano, M. A.; Szleifer, I. Molecular dynamics simulation of lysozyme adsorption/desorption on hydrophobic surfaces. *J. Phys. Chem. B* **2012**, *116*, 10189−10194.

(50) Samieegohar, M.; Ma, H.; Sha, F.; Jahan Sajib, M. S.; Guerrero-García, G. I.; Wei, T. Understanding the interfacial behavior of

lysozyme on Au (111) surfaces with multiscale simulations. *Appl. Phys. Lett.* **2017**, *110*, 073703.

(51) Nakano, C. M.; Ma, H.; Wei, T. Study of lysozyme mobility and binding free energy during adsorption on a graphene surface. *Appl. Phys. Lett.* **2015**, *106*, 153701.

(52) Wei, T.; Ma, H.; Nakano, A. Decaheme cytochrome MtrF adsorption and electron transfer on gold surface. *J. Phys. Chem. Lett.* **2016**, *7*, 929−936.

(53) Gao, W.; She, F.; Zhang, J.; Dumée, L. F.; He, L.; Hodgson, P. D.; Kong, L. Understanding water and ion transport behaviour and permeability through poly (amide) thin film composite membrane. *J. Membr. Sci.* **2015**, *487*, 32−39.

(54) Takizawa, Y.; Inukai, S.; Araki, T.; Cruz-Silva, R.; Uemura, N.; Morelos-Gomez, A.; Ortiz-Medina, J.; Tejima, S.; Takeuchi, K.; Kawaguchi, T.; Noguchi, T.; Hayashi, T.; Terrones, M.; Endo, M. Antiorganic fouling and low-protein adhesion on reverse-osmosis membranes made of carbon nanotubes and polyamide nano-composite. *ACS Appl. Mater. Interfaces* **2017**, *9*, 32192−32201.

(55) Wang, L.; Dumont, R. S.; Dickson, J. M. Molecular dynamic simulations of pressure-driven water transport through polyamide nanofiltration membranes at different membrane densities. *RSC Adv.* **2016**, *6*, 63586−63596.

(56) Li, K.; Liu, L.; Wu, H.; Li, S.; Yu, C.; Zhou, Y.; Huang, W.; Yan, D. Understanding the temperature effect on transport dynamics and structures in polyamide reverse osmosis system via molecular dynamics simulations. *Phys. Chem. Chem. Phys.* **2018**, *20*, 29996−30005.

(57) Sagle, A.; Freeman, B. Fundamentals of membranes for water treatment. *The Future of Desalination in Texas*, report number 363 2004, *2* (363), 137.

(58) Park, H.-G.; Kwon, Y.-N. Long-Term Stability of Low-Pressure Reverse Osmosis (RO) Membrane Operation—A Pilot Scale Study. *Water* **2018**, *10*, 93.

(59) Wimalawansa, S. J. Purification of contaminated water with reverse osmosis: effective solution of providing clean water for human needs in developing countries. *Int. J. Emerging Technol. Adv. Eng.* **2013**, *3*, 75−89.

(60) Hobbs, C.; Taylor, J.; Hong, S. Effect of surface roughness on fouling of RO and NF membranes during filtration of a high organic surficial groundwater. *J. Water Supply Res. T.* **2006**, *55*, 559−570.

(61) Elimelech, M.; Zhu, X.; Childress, A. E.; Hong, S. Role of membrane surface morphology in colloidal fouling of cellulose acetate and composite aromatic polyamide reverse osmosis membranes. *J. Membr. Sci.* **1997**, *127*, 101−109.

(62) Khan, M. M. T.; Stewart, P. S.; Moll, D. J.; Mickols, W. E.; Nelson, S. E.; Camper, A. K. Characterization and effect of biofouling on polyamide reverse osmosis and nanofiltration membrane surfaces. *Biofouling* **2011**, *27*, 173−183.

(63) Myat, D. T.; Stewart, M. B.; Mergen, M.; Zhao, O.; Orbell, J. D.; Gray, S. Experimental and computational investigations of the interactions between model organic compounds and subsequent membrane fouling. *Water Res.* **2014**, *48*, 108−118.

(64) Shekhar, A.; Kalia, R. K.; Nakano, A.; Vashishta, P.; Alm, C. K.; Malthe-Sørenssen, A. Universal stretched exponential relaxation in nanoconfined water. *Appl. Phys. Lett.* **2014**, *105*, 161907.

(65) Milischuk, A. A.; Krewald, V.; Ladanyi, B. M. Water dynamics in silica nanopores: The self-intermediate scattering functions. *J. Chem. Phys.* **2012**, *136*, 224704.

(66) Bucher, D.; Guidoni, L.; Carloni, P.; Rothlisberger, U. Coordination numbers of K+ and Na+ ions inside the selectivity filter of the KcsA potassium channel: Insights from first principles molecular dynamics. *Biophys. J.* **2010**, *98*, L47−L49.

(67) Busch, S.; Pardo, L. C.; O'Dell, W. B.; Bruce, C. D.; Lorenz, C. D.; McLain, S. E. On the structure of water and chloride ion interactions with a peptide backbone in solution. *Phys. Chem. Chem. Phys.* **2013**, *15*, 21023−21033.

(68) Hong, Z.-H.; Hwang, S.-F.; Fang, T.-H. Atomic-level stress calculation and surface roughness of film deposition process using molecular dynamics simulation. *Comput. Mater. Sci.* **2010**, *48*, 520−528.